Phase stability, electronic structure, and optical properties of indium oxide polytypes

S. Zh. Karazhanov,[1,2] P. Ravindran,[1] P. Vajeeston,[1] A. Ulyashin,[3] T. G. Finstad,[4] and H. Fjellvåg[1]
[1]*Department of Chemistry, University of Oslo, P.O. Box 1033 Blindern, N-0315 Oslo, Norway*
[2]*Physical-Technical Institute, 2B Mavlyanov Street, Tashkent 700084, Uzbekistan*
[3]*Institute for Energy Technology, P.O. Box 40, NO-2027 Kjeller, Norway*
[4]*Department of Physics, University of Oslo, P.O. Box 1048 Blindern, N-0316 Oslo, Norway*
(Received 17 January 2007; revised manuscript received 13 July 2007; published 29 August 2007)

Structural phase stability, electronic structure, optical properties, and high-pressure behavior of polytypes of In_2O_3 in three space group symmetries $I2_13$, $Ia\bar{3}$, and $R\bar{3}$ are studied by first-principles density-functional calculations. From structural optimization based on total energy calculations, lattice and positional parameters have been established, which are found to be in good agreement with the corresponding experimental data except for $I2_13$, where the symmetry analysis for optimized structure indicates that it arrived at the $Ia\bar{3}$ phase. In_2O_3 of space group symmetry $Ia\bar{3}$ is found to undergo a pressure-induced phase transition to the $R\bar{3}$ phase at pressures around 3.8 GPa. From the analysis of band structure coming out from the calculations within the local density and generalized gradient approximations, it is found that In_2O_3 of space group symmetry $I2_13$ and $R\bar{3}$ are indirect band gap semiconductors, while the other phase of space group $Ia\bar{3}$ is having direct band gap. The calculated carrier effective masses for all these three phases are compared with available experimental and theoretical values. From charge-density and electron localization function analysis, it is found that these phases have dominant ionic bonding with noticeable covalent interaction between indium and oxygen. The magnitudes of the absorption and reflection coefficients for In_2O_3 with space groups $Ia\bar{3}$ and $R\bar{3}$ are small in the energy range 0–5 eV, indicating that these phases can be regarded and classified as transparent.

DOI: 10.1103/PhysRevB.76.075129 PACS number(s): 71.15.−m, 71.22.+i

I. INTRODUCTION

Transparent conducting oxides (TCOs) have increased scientific interest because of their many useful features such as transparency in the visible spectrum of incident light and high electrical conductivity. The main interest for the investigation of TCO is their extensive applications such as window layers in solar cells, sensors, front electrodes in flat panel displays, low emissive windows, electrochromic materials in rare-view mirrors of automobiles, smart windows, etc. Investigations on TCO have lead to the formation of a new field in optoelectronic device technology called transparent electronics or invisible electronics.[1–7] Here, a combination of *n*- and *p*-type homo-*p*-*n*-junction based on TCO could lead to a functional window, which transmits visible portion of solar radiation and, at the same time, generates electricity by the absorption of the ultraviolet part of sunlight.[6]

One of the materials widely used as TCO is Sn doped In_2O_3 (commonly referred to as ITO). In_2O_3 can exist in three different phases characterized by space group symmetries $I2_13$, $Ia\bar{3}$, and $R\bar{3}$, which we refer to throughout the paper as phases In_2O_3-I, -II, and -III, respectively. Among them, the In_2O_3-I is rarely studied. Only a few papers[8] are available on crystal structure studies of this phase. In_2O_3-II with band gap of E_g=3.7 eV (Ref. 9) is widely studied both theoretically and experimentally. Until recently, In_2O_3-III was also rarely studied because it is a high-pressure phase and therefore not easily available. However, recent works have changed this situation. Nanoparticles of In_2O_3 in rhombohedral structure have been synthesized by hydrothermal method, followed by postannealing at moderate temperatures and pressures.[10] Phase selective growth of this phase was also demonstrated[11] by means of metal organic chemical vapor deposition method at high substrate temperatures (>550 °C) and low (>4 μmol/min) trimethylindium flow rates. Furthermore, it is found[12] that this phase can be formed upon annealing in air at >550 °C from the amorphous indium zinc oxide.

The electronic structures of ideal and defective In_2O_3 with oxygen vacancies have been studied by the discrete variational $X\alpha$ method, and it was found[9] that vacancy levels appear in the band gap. From comparative analysis of electronic structure of In_2O_3, ZnO, and SnO_2, it was shown that they possess a unique feature that the holes are heavier than conduction band (CB) electrons.[13] *Ab initio* studies of In_2X_3 (X=O,S,Se,Te) using the tight-binding linear muffin-tin orbital (LMTO) method show that compression of the lattice increases the band gap.[14] Further, this method has been applied to analyze the x-ray photoelectron, bremsstrahlung isochromat, and optical spectra of In_2O_3 and ITO. Based on band-structure calculations for In_2O_3 and ITO[15,16] using the density-functional full-potential (FP) LMTO and full-potential linearized augmented plane wave method, criteria for transparent conducting behavior have been formulated, and it is found that position, dispersion, and character of the lowest conduction band are responsible for electro-optical properties. By a systematic study[17] using the density-functional theory (DFT) within the local density (LDA) and generalized gradient approximations (GGA) with the multiorbital mean-field Hubbard potential (LDA+U and GGA+U), it is found that the band gap of In_2O_3-II calculated within pure LDA and GGA is direct, while that calculated within LDA+U and GGA+U with and without the spin-orbit coupling is indirect. The latter approximation is found to correct also energy location of the In 4*d* electrons. From first-principles molecular orbital calculations, native donors such as the oxygen vacancy (V_O), indium interstitial (In_i) and the

V_O-In_i complex were studied[18] in undoped In_2O_3, and it is found that In_i generates a shallow donor level, V_O-In_i creates even shallower level, while V_O forms a very deep donor level and facilitates emergence of In_i.

Schematic energy band model for ITO was constructed[19] based on x-ray photoelectron spectroscopy (XPS) studies. A systematic study of the electronic structure as well as optical and transport properties for cubic ITO was performed[20–22] using the *ab initio* software CRYSTAL. Dependence of carrier mobility and film resistance with carrier concentration in the range 10^{18}–10^{22} cm^{-3} (Ref. 21), optical spectra in the energy range 0.0–3.1 eV (Ref. 22), and carrier concentrations of 10^{18}–10^{22} cm^{-3} (Ref. 20) were analyzed, and good agreement with experimental data was achieved. The electronic band structure and the cohesive energies of $In_4Sn_3O_{12}$ and In_5SnSbO_{12} were calculated by DFT within GGA, and it is found[23] that incorporation of Sb into the $In_4Sn_3O_{12}$ matrix broadens the conduction band.

There still exist some points which should be clarified: (i) Among the In_2O_3-I, -II, and -III polymorphs, only In_2O_3-II is widely studied; (ii) charge density, Bader and Voronoi charges, as well as electron localization function analysis were not performed; (iii) structural properties of In_2O_3-I, -II, and -III and possibility of phase transition between these phases were not studied; (iv) optical spectra are available only for films, and In_2O_3-II and -III in a narrow energy range 0–6 eV; and (v) there are no experimentally measured effective masses for In_2O_3-I and -III. The aim of this paper is to study the structural, electronic, and optical properties of In_2O_3-I, -II, and -III by *ab initio* calculations.

II. STRUCTURAL ASPECTS AND COMPUTATIONAL DETAILS

A. Crystal structures

Crystal structures (Fig. 1) and lattice parameters (Table I) for In_2O_3-I, -II, and -III taken from Ref. 24 are used as input for the structural optimization. In all the three polymorphs, the coordination is sixfold for In atoms and fourfold for O atoms.

In_2O_3-I crystallizes in a cubic bixbyite-type structure (space group No. 199) with 8 f.u. per unit cell, with those containing three types of In and two types of O atoms occupying 8*a*, 12*b*, 12*b*, 24*c*, and 24*c* Wyckoff positions, respectively. In Fig. 1, the three types of In atoms are indicated by different colors and all are surrounded by oxygen in trigonal biprism coordination. The In_2O_3-II phase also crystallizes in a cubic bixbyite-type structure with space group No. 206 and 8 f.u. per unit cell. Distinct from In_2O_3-I, it has different atomic arrangements and bond lengths, and consists of two types of In (they are surrounded by oxygen in the octahedral and trigonal prismatic coordinations alternatively, as shown in Fig. 1) and one type of O atoms located at Wyckoff positions 8*b*, 24*d*, and 48*e*, respectively. It may be noted that the polyhedra surrounding the two types of In atoms differ from those of In_2O_3-I. In_2O_3-III is of corundum structure with 2 f.u. per unit cell (space group No. 167). It consists of one type of In (surrounded by oxygen in trigonal biprism coordination) and one type of O atoms occupying 12*c* and 18*e* Wyckoff positions, respectively. This is a high-pressure phase[10] and, consequently, has been rarely produced, but it has been claimed[10,11] that the stability and conductivity of this phase should be favorable to that of cubic phase.

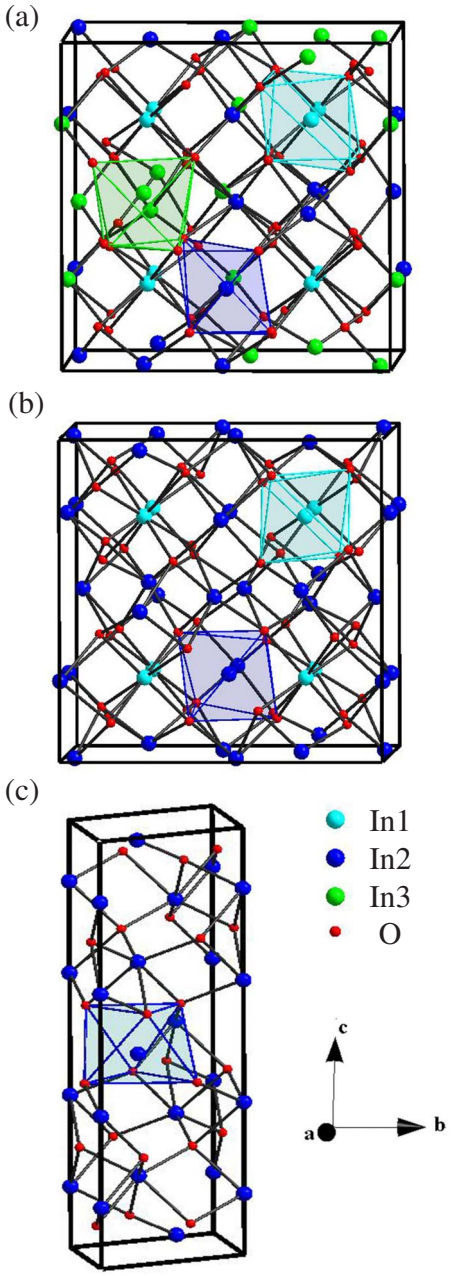

FIG. 1. (Color online) Crystal structures of (a) In_2O_3-I (experimental structural parameters), (b) In_2O_3-II, and (c) In_2O_3-III. Different types of In atoms are marked by different colors.

B. Computational details

The band-structure calculations have been performed using the VASP projector-augmented wave (PAW) package,[27] which calculates the Kohn-Sham eigenvalues in the framework of DFT within LDA. For the exchange-correlation potential and energy, we have used the Perdew-Zunger

TABLE I. Equilibrium lattice parameters (a, b, and c) and volumes (V), positional parameters, bulk modulus (B_0), and its pressure derivative (B_0') for different phases of In_2O_3 derived from the total energies obtained from present DFT calculations. Values given in parentheses refer to experimental data (Ref. 24).

Compound space group	Unit cell (Å)	Atom	Site	x	y	z	B_0 (GPa)	B_0'
In_2O_3-I	$a=10.080$ (10.120)[a]	In1	8a	0.2500 (0.2500)	0.2500 (0.2500)	0.2500 (0.2500)	172.44	4.79
$I2_13$	$b=10.080$ (10.120)[a]	In2	12b	0.0335 (0.0210)	0.0000 (0.0000)	0.2500 (0.2500)		
	$c=10.080$ (10.120)[a]	In3	12b	0.5338 (0.5420)	0.0000 (0.0000)	0.2500 (0.2500)		
	$V=1024.26$ (1036.43)[a] Å^3	O1	24c	0.1182 (0.1250)	0.1099 (0.1350)	0.3456 (0.3950)		
		O2	24c	0.1543 (0.1000)	0.3821 (0.3580)	0.3901 (0.3730)		
In_2O_3-II	$a=10.077$ (10.117)[b]	In1	8b	0.2500 (0.2500)	0.2500 (0.2500)	0.2500 (0.2500)	172.87	4.75
$Ia\bar{3}$	$b=10.077$ (10.117)[b]	In2	24d	0.4665 (0.4668)	0.0000 (0.0000)	0.2500 (0.2500)		
	$c=10.077$ (10.117)[b]	O	48e	0.3900 (0.3905)	0.1544 (0.1529)	0.3820 (0.3832)		
	$V=1023.28$ (1035.51)[b] Å^3							
In_2O_3-III	$a=5.4928$ (5.4870)[c]	In	12c	0.0000 (0.0000)	0.0000 (0.0000)	0.3576 (0.3573)	183.61	4.62
$R\bar{3}c$	$b=5.4928$ (5.4870)[c]	O	18e	0.2961 (0.2980)	0.0000 (0.0000)	0.2500 (0.25000)		
	$c=14.4242$ (14.5100)[c]							
	$V=376.89$ (378.33)[c] Å^3							

[a]Experimental values from Ref. 8.
[b]Experimental values from Ref. 25.
[c]Experimental values from Refs. 10 and 26.

interpolation[28] of the many-body calculations of Ceperley and Alder.[29] To clarify whether In_2O_3-II possesses direct or indirect band gap, we have performed additional calculations using generalized gradient approximations (GGA) where Perdew-Burke-Ernzerhof exchange-correlation functional[30] has been used. The interaction between electrons and atomic cores was described by means of non-norm-conserving pseudopotentials implemented in the VASP package. The pseudopotentials are generated in accordance with the PAW method.[31,32] The use of the PAW pseudopotentials addresses the problem of the inadequate description of the wave functions in the core region—a problem common to all pseudopotential approaches.[33] The application of the pseudopotentials allow us to construct orthonormalized all-electron-like wave functions for the In 4d and 5s, and O 2s and 2p valence electrons. Except spin-orbit coupling, all the other relativistic effects are included in the present calculations.

The diagonal elements of the effective mass tensor for the conduction band (CB) electrons are calculated by

$$\frac{1}{m_c(\mathbf{k})} = \frac{1}{\hbar^2}\frac{\partial^2 E(\mathbf{k})}{\partial \mathbf{k}^2} \tag{1}$$

in different directions in the $\mathbf{k}$ space from the Γ point toward the other high-symmetry points in the Brillouin zone of In_2O_3-I, -II, and -III. We use this to give an indication of the conduction, since the CB minimum of the band dispersions of all the compounds considered [see Sec. III B] are located at the Γ point of the Brillouin zone. The band edge energies $E(\mathbf{k})$ have been extracted from DFT calculations, and ninth order polynomial fitting has been performed. From the fitted polynomial, second order derivative was calculated, which was used in the effective mass calculations in Eq. (1). We have studied the effective masses along the crystallographic directions [001], [011], and [111] corresponding to the directions $\Gamma \rightarrow H$, $\Gamma \rightarrow N$, and $\Gamma \rightarrow P$, respectively, for In_2O_3-I and -II and $\Gamma \rightarrow L$, $\Gamma \rightarrow F$, and $\Gamma \rightarrow Z$ for In_2O_3-III.

The equilibrium lattice parameters and bulk modulus for In_2O_3-I, -II, and -III are determined from the total energies obtained as a function of volume calculated including cell shape as well as atom position relaxations into the computation using the universal equation of state fitting.[34] The calculations have been performed on a Γ centered $10\times10\times10$ $\mathbf{k}$ grid in the entire Brillouin zone.

The imaginary part of the optical dielectric function $\epsilon_2(\omega)$ has been derived from DFT results by summing interband transitions from occupied to unoccupied states for energies much higher than those of phonons. The real part of the dielectric function $\epsilon_1(\omega)$ is calculated using the Kramers-Kronig transformation. The knowledge of both the real and imaginary parts of the dielectric tensor allows one to calculate other important optical parameters. In this paper, we present and analyze the reflectivity $R(\omega)$, the absorption coefficient $\alpha(\omega)$, the refractive index $n(\omega)$, and the extinction coefficient $k(\omega)$. More details about the optical calculations were discussed in Refs. 35 and 36.

For simplification of analysis of the optical spectra, the labels E_0, E_1, E_2, d_1, and d_2 have been used. Here, the subscript 0 in E refers to transitions occurring at Γ, 1 for transitions at points in the [111] direction, and 2 for transitions in the [100] direction of the $\mathbf{k}$ space.[37] These notations are used based on those of Ref. 37 to describe the reflectivity spectra of semiconductors of wurtzite and zinc blende structures.

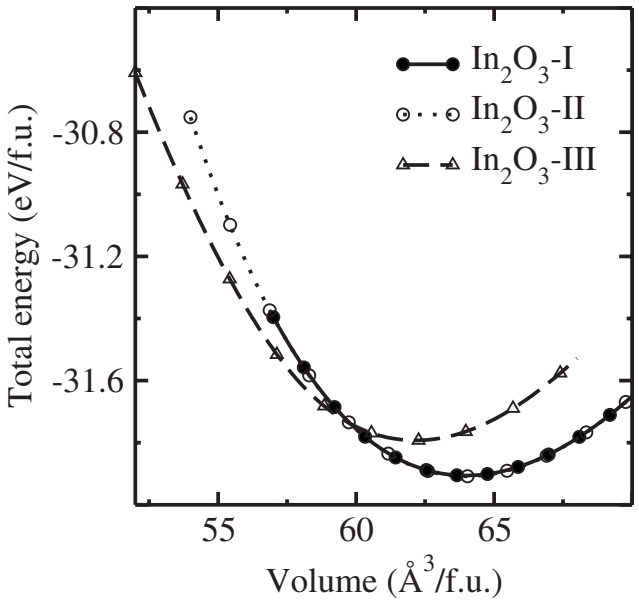

FIG. 2. Dependence of total energy E_{tot} with cell volume V per formula unit cell for In_2O_3-I, In_2O_3-II, and In_2O_3-III.

III. RESULTS AND DISCUSSION

A. Ground-state properties

Using the experimentally determined crystal structure information as input, structural optimization has been performed for In_2O_3-I, -II, and -III. Positional and lattice parameters derived from the DFT calculations for the equilibrium lattices are given in Table I together with the experimentally determined values. Analysis of the Table I shows that deviation of the calculated equilibrium volumes are $<1.2\%$ of the experimentally determined values, which indicates that the theoretical calculations are reliable in predicting structural parameters for such complex systems. Furthermore, symmetry of the thus optimized lattices is checked for In_2O_3-I, -II, and -III, and it is found that it is the same as that of the corresponding experimentally determined one. Although for the In_2O_3 phases studied in this paper the calculated and experimentally determined lattice parameters do not deviate much from each other, such a structural study is still needed because the optimized atomic positions deviate from experiment for In_2O_3-I.

Analysis of Fig. 2 shows that E_{tot}^{min} for In_2O_3-III is larger than that of In_2O_3-I and -II. Total energies, volumes, and crystal structures for In_2O_3-I and -II are nearly the same and the difference is within the accuracy of the calculations. So, In_2O_3-I can be regarded as distorted In_2O_3-II, and small variation of temperature or pressure can cause structural transformation of In_2O_3-I into In_2O_3-II. The transition is well demonstrated in Table II about atomic distances of the relaxed and unrelaxed lattices of In_2O_3-I, -II, and -III. It is seen that after optimization, positional parameters for In2 and In3 atoms of In_2O_3 become almost the same when we use LDA and exactly the same for GGA. Furthermore, the positional parameters obtained from calculations within GGA are closer to experimental data than the LDA derived values. This result is in agreement with the general opinion that structural optimization using GGA is more preferable than that using LDA. However, as we noted above, underestimation of the equilibrium volume even within LDA is $<1.2\%$, which indicates that the relaxation within LDA, in this particular case, shall not lead to large deviations of electronic structure and optical spectra from experimental values except for In_2O_3-I. Due to the difference in the optimized and experimental positional parameters for In_2O_3-I, there is large difference in the electronic structure and optical properties between experimental and theoretically optimized structures for this phase.

From Fig. 2, it is seen that equilibrium volume for In_2O_3-III is smaller, but the total energy is higher than that for In_2O_3-II, which indicates that In_2O_3-III is less stable than In_2O_3-II. Furthermore, at lower volumes, and, respectively, higher pressures, the dependence $E_{tot}(V)$ for In_2O_3-III crosses that for In_2O_3-II. It indicates that, upon compression, In_2O_3-II can be transformed into In_2O_3-III. In order to estimate the pressure value for the transitions from In_2O_3-II to -III, we have plotted the dependence of Gibbs free energy (defined as $G=U+PV$, where U is the total energy for the particular pressure P at volume V) difference (ΔG) as a function of the applied pressure (Fig. 3). The pressure value at which $\Delta G=0$ is the transition pressure at the structural phase transition point. According to our findings in Fig. 3, the pressure-induced phase transitions from In_2O_3-II to -III occurs at $P=3.83$ GPa.

TABLE II. Interatomic distances (multiplicity in parentheses) for relaxed and unrelaxed lattices of In_2O_3-I, -II, and -III calculated by DFT within the LDA and GGA. The interatomic distances of the experimentally determined crystal structures correspond to unrelaxed lattices.

Phase	In_2O_3-I (expt.)	In_2O_3-I (LDA)	In_2O_3-I (GGA)	In_2O_3-II (expt.)	In_2O_3-II (LDA)	In_2O_3-III (expt.)	In_2O_3-III (LDA)
In1-O1	2.247 (3×)	2.166 (3×)	2.213 (3×)	2.191 (6×)	2.166 (6×)	2.116 (3×)	2.120 (3×)
In1-O1	2.260 (3×)	2.167 (3×)	2.213 (3×)			2.258 (3×)	2.248 (3×)
In2-O1	2.232 (2×)	2.121 (2×)	2.165 (2×)	2.120 (2×)	2.118 (2×)		
In2-O2	2.268 (2×)	2.186 (2×)	2.235 (2×)	2.192 (2×)	2.187 (2×)		
In2-O2	2.273 (2×)	2.212 (2×)	2.255 (2×)	2.210 (2×)	2.211 (2×)		
In3-O1	2.264 (2×)	2.120 (2×)	2.165 (2×)				
In3-O1	2.285 (2×)	2.186 (2×)	2.235 (2×)				
In3-O2	2.261 (2×)	2.211 (2×)	2.255 (2×)				

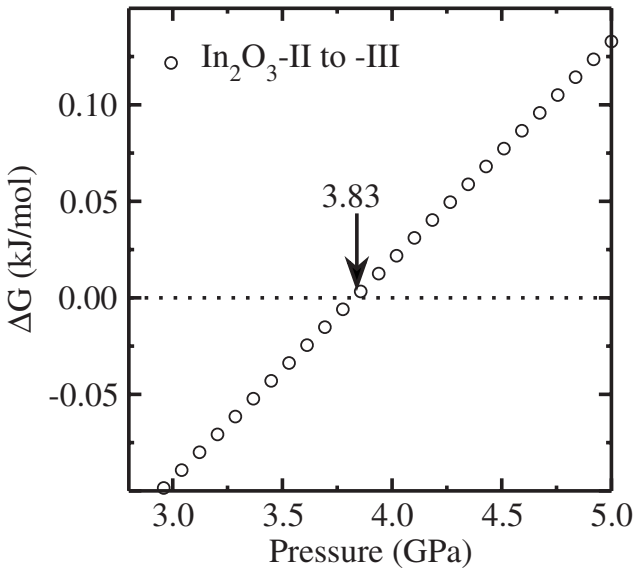

FIG. 3. Gibbs free-energy difference for In_2O_3-III relative to In_2O_3-II (open circles) as a function of the applied pressure. Structural phase transition point is marked with an arrow and the corresponding pressure value (in GPa) is also stated.

The pressure-induced structural transition is well demonstrated in the total energy variation with volume curves (see Fig. 2), and from that, the dependence of the cell volume on applied pressure is derived (Fig. 4). It is seen that the volume shrinkage at the transition pressure is 1.72 $Å^3$. The phase transition In_2O_3-II-to-III is accompanied by breaking and transformations of chemical bonds between atoms and reconstruction of anion and cation sublattices.

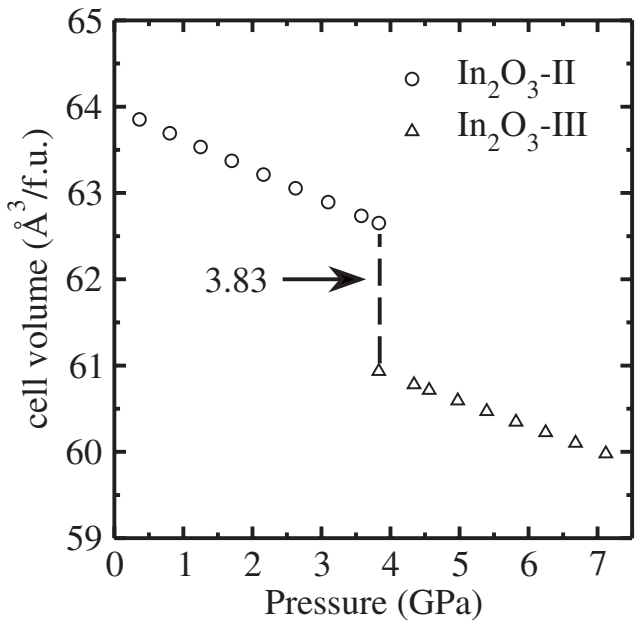

FIG. 4. Calculated cell volume as a function of pressure for In_2O_3-II and -III. The pressure-induced phase transition point is marked with an arrow and the corresponding pressure value at the transition point (in GPa) is also stated.

Phase transition from In_2O_3-II to -III was studied experimentally in the literature before. However, the reported transition pressure value from different experimental studies differs noticeably. In Ref. 38, such a transition has been demonstrated experimentally at 6.5 GPa and 1250 °C. However, at pressures up to 6 GPa and temperatures 550, 1000, and 1450 °C, In_2O_3 has been retained[39] in phase -II. According to experiments of Ref. 26, the mixture of In_2O_3 and Co possesses the same structure as In_2O_3-III. The experimental results from Ref. 26 for pure In_2O_3 show that the formation of In_2O_3-III was possible at 800 °C provided that the sample is initially preheated at 1250 °C. Without the preheating, formation of In_2O_3-III occurred at 1000 °C only. In contrast to the experimental report from Refs. 26, 38, and 39, the pressure-induced phase transition obtained in the present work is small and, however, it corresponds to 0 K. It may be noted that the phase selective growth of In_2O_3-III in the experiments of Ref. 11 always occurred at very low pressures (20 kPa).

Bulk modulus is the parameter characterizing the compressibility of a solid. The bulk modulus of In_2O_3-III is larger than those of In_2O_3-I and -II. Consequently, the phases -I and -II are more easily compressible than In_2O_3-III. No experimental data on bulk modulus values for pure In_2O_3-I, -II, and -III have been reported so far. So, the calculated bulk modulus values are compared to 99±32 GPa of ITO films.[40] It is seen that our calculated bulk moduli for In_2O_3 phases (Table I) are much larger than that for the ITO films and, consequently, the pure In_2O_3 phases are hardly compressible than the Sn doped In_2O_3 films.

B. Band structure

For a better understanding of the electronic and optical properties and chemical bonding of the polytypes of indium oxide, the analysis of band structures can be quite helpful. Band structures for In_2O_3-I, -II, and -III calculated in this work are presented in Fig. 5. Although we noted above that In_2O_3-I is distorted In_2O_3-II, we still plotted band structure for both In_2O_3-I and -II to demonstrate how lattice distortion can drastically change the band structure. For example, a well distinct band region is seen in the bottom of the CB of In_2O_3-I [Fig. 5(a)] compared with other two polymorphs. This distinct band region is split from the rest of the CB, and it is located in the energy range 0.009–2.391 eV above the topmost valence band (VB). This band region can be called as intermediate band (IB). Since IB is well dispersive, recombination of electrons and holes through this band is not expected to be very high. As this band region is completely empty, it can be useful for photoemission of electrons from VB to the IB. The small difference in total energy of In_2O_3-I and -II and large difference in the band features at the CB minimum in these two modifications indicate that one can drastically change the optical properties by different preparatory conditions by stabilization of different proportions of these two phases.

Despite the large difference in crystal structures, In_2O_3-I, -II, and -III have some similar features. Particularly, the bottommost CB of In_2O_3-I, -II, and -III is dispersive and is

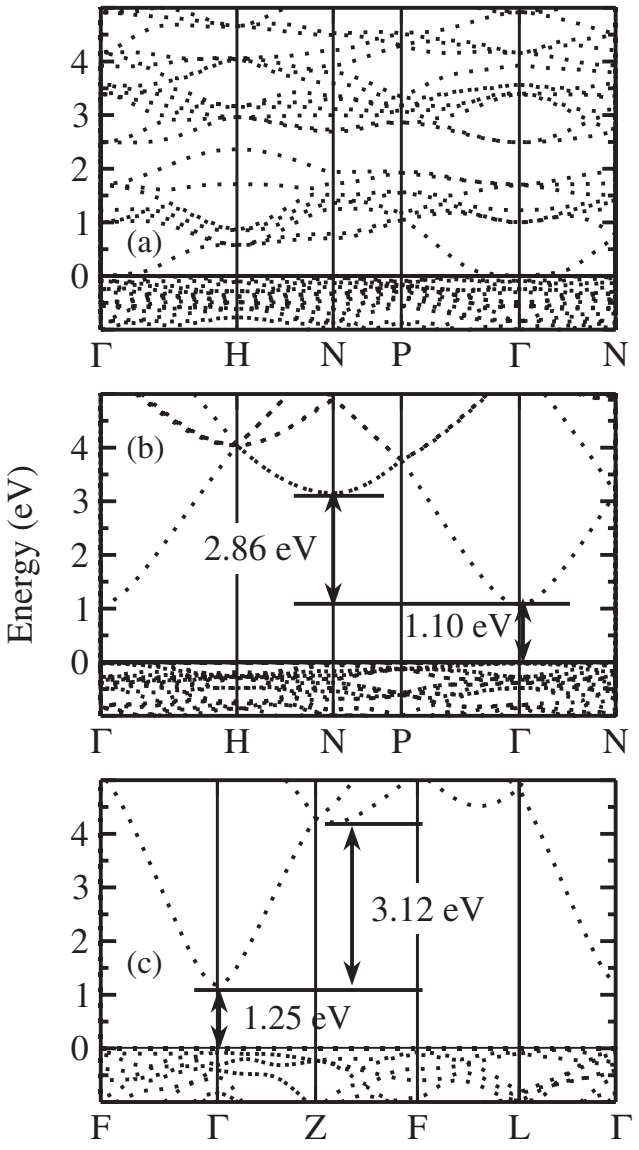

FIG. 5. Band structure for (a) unrelaxed In_2O_3-I, (b) In_2O_3-II, and (c) In_2O_3-III near the VB maximum and CB minimum. The Fermi level is set to zero.

located at the Γ point, while the topmost VB is flat, which are the important properties inherent to TCO materials. The VB consists of three regions in all the three phases. The lowest one is located below −15 eV from the topmost VB. The bands at the intermediate energy region is located between −14 and −10 eV. Both these band energy regions are very narrow, while the topmost VB region is quite broad. The VB maximum is located at Γ point for In_2O_3-I and -II and at *L* point for In_2O_3-III. Consequently, one can conclude that the In_2O_3-III is an indirect band gap material, while In_2O_3-I and -II are direct band gap materials.

The direct band gaps (E_g^{dir}) coming out from the LDA calculations are presented in Table III along with the experimentally determined values. Analysis of Table III shows that the calculated E_g^{dir} for In_2O_3-I, -II, and -III are underestimated due to the well-known problem of the DFT. Experimental data for the band gap of In_2O_3-I are not yet available. Our calculated E_g^{dir} for In_2O_3-II is in good agreement with 0.9 eV,[13] 1.0 eV,[15] and <1.0 eV,[14] reported from DFT calculations. The second band gap (E_g^s), which is the energy difference between the two lowest CBs, has been calculated. We found that E_g^s of In_2O_3-III is larger than that of In_2O_3-I and -II. So, one can expect transparency in a wider energy range of the solar spectra from In_2O_3-III than from In_2O_3-I and -II.

The character (direct or indirect) and value of the band gap are important factors for the characterization of TCO materials. Until recently, band-structure results obtained from different theoretical studies of In_2O_3-II have been controversial. From the band-structure calculations using the LMTO method within the atomic sphere approximation (ASA) based on the LDA, it is found[14] that the band gap of In_2O_3-II is indirect with CB minimum at the Γ point and VB maximum at *H* point. However, DFT calculations of Refs. 13, 15, and 42 show that the band gap of In_2O_3-II is direct with CB minimum and VB maximum located at the Γ point. The band gap value of 1.0 eV was found for experimental lattice constant and 1.5 eV for theoretically determined lattice constants.[15] Recent systematic study of Ref. 17 by DFT calculations within LDA+*U* and GGA+*U* has shed light on the problem. It is found that the band gap of In_2O_3-II calculated within pure LDA and GGA is direct, while that calculated within LDA+*U* and GGA+*U* for $U-J=7$ eV is indirect. Our results given in Table III are in agreement with these findings. We have calculated the band structure of In_2O_3-II using the theoretically and experimentally determined lattice constants within LDA and GGA. It shows that the CB minimum and VB maximum are located at the Γ point. Hence, we conclude that the band gap of In_2O_3-II calculated within pure LDA and GGA is direct. Our experience shows that the indirect band gap predicted by LMTO method is associated with the use of ASA in the calculation.

From room temperature fundamental absorption edge studies, it was found[43] that direct and indirect band gaps of single crystal In_2O_3-II are 3.750 and 2.619 eV, respectively. Similar band gap values have been found[44] from absorption measurements for In_2O_3 films, which decreased with increasing film thickness from 2.65 eV for 100 nm to 2.40 eV for 400 nm. The band gap also decreased with increasing deposition temperature from 2.50 eV at 20 K to 2.30 eV at 270 K. Band gap reduction from 2.46 to 2.30 eV was reported to be caused also by increase of the annealing temperature from 200 to 500 K. From these reports, it appears that structural defects play an important role in defining the band gap of In_2O_3 and hence optical properties.

C. Density of states

Insight into the bonding interaction between constituents can be obtained from the site and orbital projected partial density of states (DOS) analysis. Moreover, analysis of the projected density of states (PDOS) gives detailed information about the origin of CB and VB electronic energy levels. Such analysis has been performed for all the phases of In_2O_3 considered in the present work (Fig. 6). The main feature in Fig. 6 is that the DOS distribution of In and O are energeti-

TABLE III. Second band gap (in parentheses) and fundamental band gap (in eV) for In_2O_3-I, -II, and -III calculated from DFT within LDA (E_g^{LDA}) and GGA (E_g^{GGA}) using the lattice parameters determined theoretically (a_0) and experimentally (a_e) along with experimentally measured values ($E_g^{expt.}$).

	E_g^{LDA}		E_g^{GGA}		
Phase	a_0	a_e	a_0	a_e	E_g^{expt}
In_2O_3-I	1.16	0.009			
In_2O_3-I	(2.93)				
In_2O_3-II	1.17	1.100	1.33	1.29	3.70[a]
	(2.86)	(2.860)	(2.80)	(2.84)	3.60[b]
					3.70[c]
In_2O_3-III		1.250			3.80[d]
		(3.120)			3.00[c]

[a]Reference 9.
[b]Reference 41.
[c]Reference 11.
[d]Reference 26.

cally not separated, indicating that the nature of chemical bonding between In and O is not pure ionic and it contains some covalency, consistent with our charge-density analysis given below. Since the basic feature of In_2O_3-I has already been discussed in the previous section, below we concentrate our attention on the analysis of In_2O_3-II and -III.

The VB of In_2O_3-II and -III can be divided into three regions. It is seen in Fig. 6 that the bands at the lowest energy region (below −15 eV from the topmost VB, we call it VB1) are mainly contributed by O 2*s* electrons with noticeable In 4*d* electrons. The bands at the intermediate energy region (located between −14 and −10 eV, we call it VB2) are basically from In 4*d* electrons with small contribution from O 2*s* and 2*p* states due to hybridization interaction. Both these band energy regions are very narrow, while the topmost VB region is quite broad.

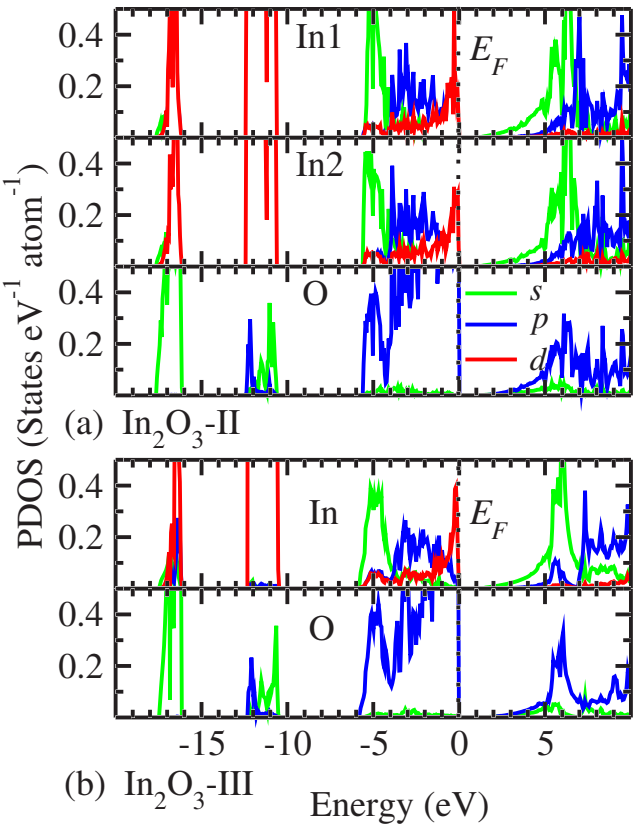

FIG. 6. (Color online) The orbital and site-projected DOS for (a) In_2O_3-II and (b) -III. The Fermi level is set to zero.

The states around −5 eV in the VB (we call VB3) are equally contributed by both In 5*s* and O 2*p* electrons. The main contribution to the topmost valence band of In_2O_3-III is from O 2*p* electrons, which has noticeable hybridization interaction with In 4*d*/5*p* electrons. The results from the PDOS analysis are in good agreement with those of previous *ab initio* calculations[9,14,15] and recent soft x-ray emission (SXE) and soft x-ray absorption (SXA) spectra measurements[45] for In_2O_3-II. The character of the topmost VB is similar to that of ZnO, which is also a transparent conducting oxide (see, e.g., Ref. 46).

The position, dispersion, and character of the lowest CB carry the key features responsible for electro-optic properties of TCO materials.[15] The bottommost CBs of In_2O_3-II and -III are mainly originating from In 5*s* electrons with finite O 2*p* contribution. Orbital and site decomposed DOS analysis is used for the detailed characterization of the contributions of electrons from *s*, p_x, p_y, p_z, d_{xy}, d_{xz}, d_{yz}, $d_{x^2-y^2}$, and d_{z^2} orbitals into the bands of particular interest. From such analysis, it is found that the topmost VB of In_2O_3-II and -III is contributed by electrons from O $2p_x$, $2p_y$, $2p_z$ orbitals, which slightly hybridized with electrons from In $4d_{xy}$, $4d_{xz}$, $4d_{yz}$ orbitals.

The origin for the CB minimum of In_2O_3-II and -III is more or less the same, and it basically originates from electrons of In 5*s* orbitals with small O 2*s*, $2p_x$, $2p_y$, and $2p_z$ character. Based on this analysis and the basic formulations suggested in Ref. 15 regarding highly dispersed and single character *s*-type band at the bottommost CB, the features that favor TCO behavior, one can conclude that In_2O_3 possesses the feature of *s*-electron based TCO.

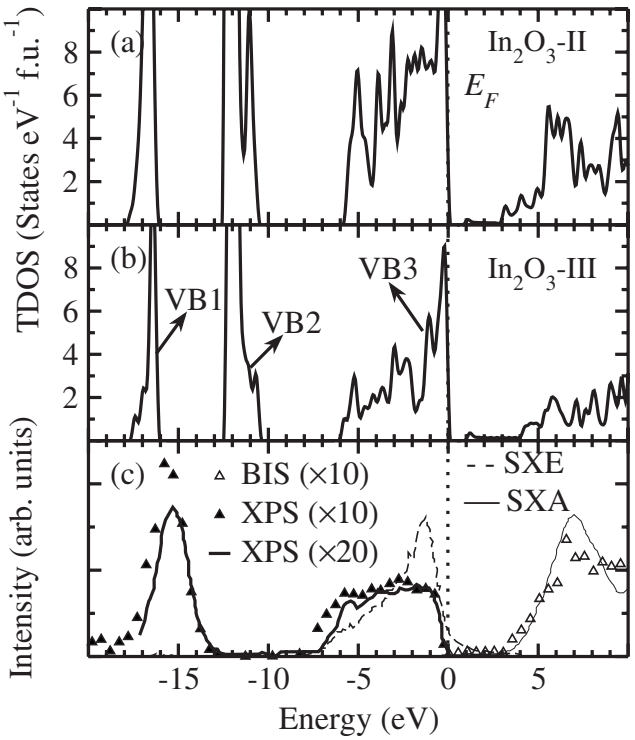

FIG. 7. Calculated total DOS for (a) In_2O_3-II and (b) -III as compared with (c) experimental data obtained from different techniques: BIS (open triangles) (Ref. 47), XPS (closed triangles, Ref. 47), XPS (thick solid lines, Ref. 48), SXE (Ref. 45), and SXA (Ref. 45). The Fermi level is set to zero.

The total DOSs for In_2O_3-II and -III are displayed in Fig. 7 along with XPS, bremsstrahlung isochromat spectroscopy (BIS), SXE, and SXA measurements. The DOSs exhibit sharper peaks than the experimental spectra, since we have not included the lifetime broadening and instrumental resolution. As noted in the Introduction, there are no experimental XPS studies available on In_2O_3-I. So, comparative analysis with experimental data has been performed only for In_2O_3-II and -III.

As noted in the previous section, there are three distinct regions in the VB of the In_2O_3 phases considered in the present work. According to the band dispersion and total DOS analysis, the widths of the band regions corresponding to VB1, VB2, and VB3 are 2.22, 1.52, and 6.38 eV for In_2O_3-I, 1.5, 1.77, and 5.46 for In_2O_3-II, and 0.81, 1.74, and 5.5 eV for In_2O_3-III, respectively. These results are in fair agreement with that of Ref. 13, where 2.33 eV for the VB2 and 5.70 eV for the topmost valence band are reported. This small discrepancy may be related to different approximations and methods used in the calculations. It should also be noted that the locations of the In $4d$ bands in In_2O_3-II and -III coming out from the DFT calculations are shifted toward higher energies and their intensity is also higher compared to experimental data [Fig. 7(d)].

Analysis of Fig. 7 shows that the widths of VB3 of In_2O_3-II and -III more or less agree with SXE measurements, which show a well-defined intensive peak closer to the topmost VB. Such a peak is smeared out in other experimental spectra shown in Fig. 7. However, the experimental spectroscopic measurements show only one peak centered around −15 eV, whereas the DFT calculation show two (VB1 and VB2) around this energy range. As mentioned in the PDOS analysis, the VB1 is mainly originating from O $2s$ electrons the photoionization cross section of which is much smaller than that of In $4d$ electrons; hence, VB1 band feature is not observed experimentally. So, the peak centered around −15 eV in the spectroscopic measurements can be concluded as the band features arising from In $4d$ electrons. However, the calculated $4d$ band (VB2) position is shifted around 2.5 eV toward the valence band maximum.

It may be noted that there is discrepancy in the XPS results of different groups. For example, the binding energy of the In $4d$ band is found to be at 14 eV in Ref. 47 and 18 eV in Ref. 48. This discrepancy may be associated with the use of different reference points in estimating the peak positions.[45] The width of the calculated VB1 band agrees with experimental data of Refs. 45, 47, and 48. Furthermore, in our calculations, these two peaks are much more intense than the topmost valence band, which disagrees with experimental data but agrees with theoretical calculations of Refs. 9 and 14. The reason for the discrepancy can be that the photoionization cross section is important in accounting for the intensity. So, only locations of the calculated total DOS have been compared with the experimental measurements. It is important to note that the pseudocore d bands are not placed correctly in systems such as ZnO (Ref. 49) and CdTe (Ref. 50) by the present type of calculations. So, one should go beyond the LDA/GGA calculations by taking into account the Coulomb correlation effects from the In $4d$ electrons through methods such as LDA+U, LDA+SIC, etc. Recent study[17] of band structure of In_2O_3 showed that within LDA +U and GGA+U calculations for $U-J=7$ eV, the In $4d$ levels have been shifted toward lower energies and split the O $2s$ band into two parts.

D. Conduction band effective masses

Effective masses characterize band dispersion and are one of the important parameters linking electronic structure with transport properties of solids. As noted above, the lowest CBs of In_2O_3-II and -III are more dispersive than the topmost VB, which means that the CB electrons are lighter than holes. Almost flat topmost VB indicates that valence electrons are tightly bound to the atoms. Consequently, the dominant intrinsic charge carriers in In_2O_3 are expected to be electrons and not holes, consistent with experimental observations. Hence, we focus on the CB electron effective masses, and the calculated results are presented in Table IV. Analysis shows that the calculated masses for In_2O_3-II and -III are almost isotropic. The observed small anisotropy can be related to the effect of p and d orbitals hybridizing with s orbitals. The deviation in the calculated effective masses from the experimentally measured values are in the range 23%–33%. This deviation can be related to the deficiency of DFT in the calculation of the eigenvalue of electrons. So, not only the band gap but also the band dispersion comes out incorrectly, and this effect is generally well pronounced in

TABLE IV. Calculated effective masses of CB electrons (in units of the free-electron mass m_0 and in the directions indicated) for In_2O_3-II and -III are compared with available experimental and calculated values.

In_2O_3-II	In_2O_3-III	ZnO
0.23 (Γ-H)	0.16 (Γ-F)	0.23 ($E\|\|c$)[a]
0.20 (Γ-N)	0.14 (Γ-L)	0.21 ($E\perp c$)[a]
0.23 (Γ-P)	0.15 (Γ-Z)	0.24[b]
0.42 (Γ-H)[c]		0.28 ($E\|\|c$)[d]
0.30 (Γ-N)[c]		0.32 ($E\perp c$)[d]
0.36 (Γ-P)[c]		0.14 ($E\|\|c$)[e]
0.30 (Γ-H)[f]		0.13 ($E\perp c$)[e]
0.36 (Γ-N)[f]		
0.41 (Γ-P)[f]		
0.30 (Γ-P)[g]		

[a]FP LMTO, Ref. 51.
[b]Experiment, Ref. 56
[c]LMTO ASA, Ref. 14.
[d]LCAO, Ref. 57.
[e]VASP-PAW, Ref. 49.
[f]DMOL3, Ref. 58
[g]Experiment, Refs. 41 and 59.

transition metal oxides (see, e.g., Refs. 51–55). Experimental data for CB electron effective masses are available for In_2O_3-II only. The calculated effective masses from the present study are compared with available experimental and other theoretical values available for In_2O_3-II and ZnO (other well-known TCO) in Table IV. Overall, the presently calculated CB effective masses for In_2O_3-II are smaller than those from experimental and other theoretical values. In particular, the masses calculated by the LMTO ASA (Ref. 14) method agree fairly with experimental data and are more anisotropic than our results.

Analysis shows that the calculated effective masses for In_2O_3-II are considerably larger than those for In_2O_3-III. Hence, carrier mobility in In_2O_3-III is expected to be larger than that in In_2O_3-II. The calculated effective masses for In_2O_3-II are much closer to experimental data than that for ZnO. This difference in accuracy of the calculated masses comes from Coulomb correlation effects, which are strong in ZnO.[49] In DFT calculations within LDA, the Zn 3d bands are located inappropriately close to the topmost VB, falsifying the band dispersion and, consequently, effective masses. As noted in the analysis of the band dispersion (Fig. 5), In 4d band is located much below the topmost VB than the 3d band in ZnO. So, Coulomb correlation effects in In_2O_3-II and -III are not as strong as that in ZnO to falsify the band masses significantly.

E. Charge-density and electron localization function analysis

For qualitative characterization of the bonding interaction between constituents, charge-density and electron localization function (ELF) analysis have been performed for In_2O_3-II (Fig. 8) and -III (Fig. 9). Analysis of the charge

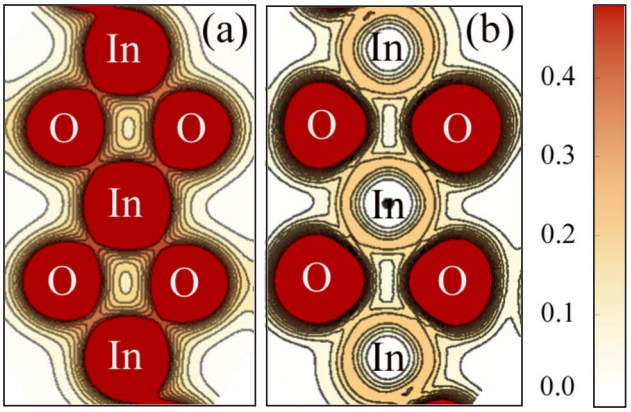

FIG. 8. (Color online) (a) Charge density (in $e/Å^3$) and (b) ELF for In_2O_3-II in the (011) plane.

distribution shows that the highest charge density is residing in the immediate vicinity of the atomic sites, reflecting the dominant ionic-type bonding. If the bonding interaction between In and O is purely ionic, one could expect negligible charge-density distribution between these ions. From Fig. 8, it is clear that there are finite charges distributed in between In and O in all the polytypes. Also, the charge around In and O atoms is not distributed spherically. These features indicate that apart from dominant ionic bonding, finite covalent-like bonding interaction is present between In and O. The observed hybridization interaction is responsible for the mixed nature of the electronic structure of this material discussed in the previous section. This suggestion is also confirmed by the Born-effective-, Bader-, and Voronoi-charge analyses in the following section.

The ELF analysis is one of the ways to measure the probability of distribution of paired electrons in solids.[60–62] It is seen from Fig. 8 that the maximum value of ELF is around O and the minimum around In atoms, which confirms the dominant ionic bonding. Between the In and O atoms, the ELF does not show any maximum value, and this indicates that there is no dominant covalent-type bonding interaction present between these atoms. However, nonspherical distri-

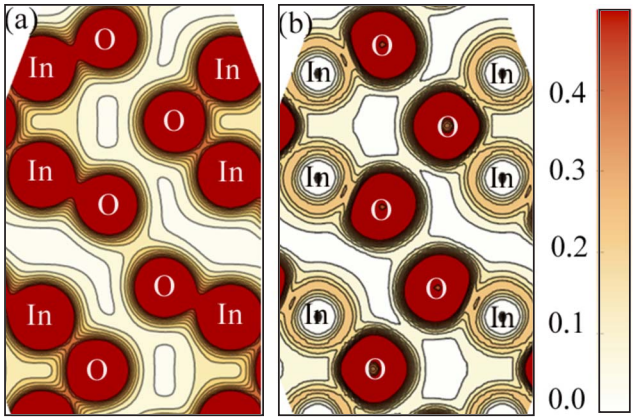

FIG. 9. (Color online) (a) Charge density (in $e/Å^3$) and (b) ELF for In_2O_3-III in the (100) plane.

TABLE V. Atomic charges (in units of the electron charge e^-) around In and O atoms calculated according to Voronoi and Bader topological analyses for In_2O_3-II and -III.

Compound	Atom	Voronoi	Bader
In_2O_3-II	In1	2.00	1.81
	In2	2.04	1.84
	O	−1.36	−1.23
In_2O_3-III	In	2.09	1.81
	O	−1.39	−1.20

bution of ELF at the O site and small but finite value of ELF in between In and O reflect the presence of non-negligible hybridization interaction between these atoms. Unlike intermetallic phases,[60] no isolated spot in the interstitial regions with high ELF is found in any of the In_2O_3 phases considered here.

F. Bader- and Voronoi-charge analyses

For quantitative characterization of chemical bonding in solids, Bader- and Voronoi-charge analyses[63–65] are widely used. In the Bader-charge analysis, each atom of a compound is surrounded by a surface (called Bader regions) that runs through the minima of the charge density and the total charge of the atom is determined by integration within the Bader region. In the Voronoi-charge analysis, each grid point of charge density is assigned to the nearest atom, but each of these distances is not scaled by the radius of each atom. So, the Voronoi charges in the present paper are used just for a sanity check. Table V presents the charges at each atomic site for In_2O_3-II and -III calculated according to the Bader and Voronoi schemes. As expected, In atoms donate electrons while O atoms accept them. Based on the amount of the transferred charges, one can conclude that chemical bonding is of dominant ionic type.

G. Born effective charges

Born effective charges (BECs) are the fundamental parameters characterizing the change in electron polarization upon displacement of atoms. They are related to microscopic electron currents produced in a system by a change of the atomic position. These currents may contribute to the BEC, which is unrelated and additional to the static electron charge carried out by the atoms during the displacement, so that BECs can be much larger than their static counterpart, i.e., higher than formal valence charge. In this case, BECs are referred to as anomalous. BECs are helpful in understanding the ferroelectric and piezoelectric properties of materials. For the present study, BECs were obtained from finite differences of macroscopic polarization induced by small displacements of the atomic sublattices using the Berry phase approach.[66,67] The calculated BEC for In_2O_3-III is given in Table VI. The formal valences for In and O are +3 and −2, respectively. The calculated BECs reflect this formal valence picture that the average diagonal components of the BEC at the In and O sites are 3.27 and −2.17, respectively. These values are slightly larger than the formal valence, indicating that there is small anomalous charge (also called dynamical charge) added to the static charge in the atoms. The diagonal components of the BEC are almost the same, indicating that the bonding interaction is more isotropic reflecting ionic-type bonding. It is seen that for In atoms, the off-diagonal elements of the BEC tensor are negligible, reflecting the ionic-type interaction. However, there are non-negligible off-diagonal elements of BEC at the O site, indicating that there is finite covalentlike bonding interaction present between O atoms. This result is in agreement with charge density and ELF analysis (Fig. 9), which demonstrates that there is finite directional bonding between nearest neighbor O atoms.

H. Optical properties

Optical properties of In_2O_3-I, -II and -III are studied. The real and imaginary parts of the optical dielectric response function, absorption coefficient, reflectivity, refractive index, and the extinction coefficients have been analyzed. Since the crystal structure of In_2O_3-I and -II is cubic, the optical spectra are isotropic along the crystallographic *a*, *b*, and *c* axes. So, only one of the components is sufficient for the analysis. We also found that the optical spectra of In_2O_3-I with optimized lattice and In_2O_3-II are almost the same.

Figure 10 presents the calculated optical spectra for In_2O_3-II and -III. All the calculated optical spectra of In_2O_3-II and -III are shifted toward lower energies compared with experimental results owing to the underestimation of the band gap in the DFT calculations. One of the ways to rectify it is to use the scissors operator technique, i.e., rigid shift of all the CB states, so that the optical spectra shall also be shifted accordingly.[55,68] The search of literature shows that experimental data are available for In_2O_3-II in Ref. 41, where reflectivity and transmittance spectra were measured by spectrophotometry at room temperature. The other optical spectra such as absorption coefficient, refractive index, and the extinction coefficient are calculated using the Kramers-Kronig relation. These five optical spectra have been compared in Fig. 10(a) with those calculated from the present band-structure results. The optical spectra of In_2O_3-II were measured[41] for a narrow energy range 0–6 eV, which contains only the E_0 peak induced by electronic transitions from

TABLE VI. Calculated Born-effective-charge-tensor elements (Z^*) for the constituents of In_2O_3-III.

Atom	*xx*	*yy*	*zz*	*xy*	*yz*	*zx*	*xz*	*zy*	*yx*
In1	3.300	3.306	3.206	0.009	0.002	0.000	0.001	0.000	0.002
O1	−2.260	−2.136	−2.130	0.098	0.432	0.186	0.257	0.308	0.432

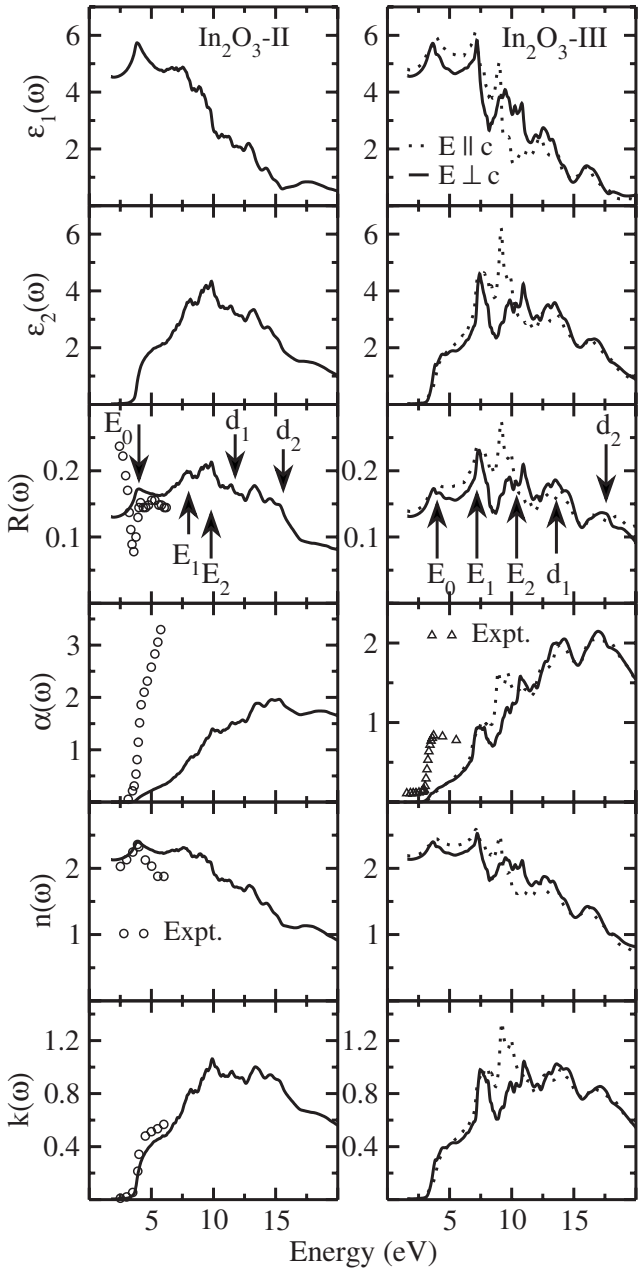

FIG. 10. Optical spectra of In_2O_3-II and In_2O_3-III for directions of the electric field (E) parallel ($E \| c$) and perpendicular ($E \perp c$) to the crystallographic c axes. Calculated imaginary parts of the optical dielectric function [$\varepsilon_2(\omega)$], absorption coefficient [$\alpha(\omega)$ in cm^{-1} multiplied by 10^{-5}], reflectivity [$R(\omega)$], refractive index [$n(\omega)$], and extinction coefficients [$k(\omega)$] for In_2O_3-II have been compared with experimental data of Ref. 41. Calculated absorption coefficient for In_2O_3-III has been compared with experimental results of Ref. 11.

the VB maximum to CB minimum occurring at the Γ point. So, in the present work, these experimental data were used for rigid shift of the calculated optical spectra toward higher energies by 1.65 eV to fit to location of the E_0 peak. Since the location of the E_0 peak is clearly seen in the spectra of $n(\omega)$, fitting was performed for $n(\omega)$. The other spectra have been shifted accordingly.

From the comparison of the calculated spectra with experimentally measured spectra, one can see that the calculated $n(\omega)$ and $k(\omega)$ agree well with experimental data. Calculated reflectivity spectra agree with experimental data only at higher energies well above the band gap. At lower energies, near the band gap, experimental reflectivity is higher than that calculated by DFT, and the experimentally observed low energy peak may be associated with excitonic effect, which is not considered in the present calculations. The calculated absorption spectra agree with the measured spectra at lower energies. However, at energies exceeding the location of the E_0 peak, the calculated absorption coefficient is found to be much smaller than the experimentally determined values. The origin for the deviation between experimental and theoretical absorption coefficient spectra is not known.

Because of the rhombohedral symmetry, there is optical anisotropy present in In_2O_3-III. The two components of the dielectric functions are calculated for In_2O_3-III corresponding to the electric field parallel $E \| c$ and perpendicular $E \perp c$ to the crystallographic c axes. The first experimental data for In_2O_3-III are already available.[11] The absorption coefficient was measured for the energy range 0–6 eV, which contains the E_0 peak. The calculated absorption spectra were shifted to 1.35 eV toward higher energies to fit the E_0 peak in order to match with experimental spectra. The other calculated optical spectra have also been shifted accordingly. The anisotropy is well pronounced at energies from ~7 to 9 eV, whereas the optical spectra are more or less isotropic at other energies considered. The locations of all the major peaks of the optical spectra corresponding to both the directions are almost the same except the E_2 peak. The magnitude of the E_2 peak at around 7.5 eV is higher for $E \| c$ and its shoulder at 8.3 eV is larger than that for $E \perp c$. Absorption and reflectivity spectra for this compound are low in the energy range 0–5 eV, indicating that it will be optically transparent.

The intensity of the calculated optical spectra differs from the experimentally measured one for both In_2O_3-II and -III. The reason of this deviation may be related to the factors such as overestimation of the momentum matrix elements, neglect of the Coulomb interaction between free electrons and holes (excitons), and local-field and finite lifetime effects. Furthermore, in the calculations of the imaginary part of the dielectric response function [$\varepsilon_2(\omega)$], only the direct optical transitions from occupied to unoccupied states are considered. Also, the lifetime effects and the experimental resolution smear out many fine features. Moreover, the experimental measurements[11,41] are made on thin films at room temperatures where one could expect considerable amount of defects which will cause changes in optical properties. However, the theoretical optical spectra are valid only for defect free single crystals at low temperatures.

IV. CONCLUSION

Structural properties, electronic structure, high-pressure behavior, and optical properties of In_2O_3 of space group symmetries $I2_13$, $Ia\bar{3}$, and $R\bar{3}$ are studied by DFT calculations. From the structural optimization using total energy cal-

culations, the equilibrium lattice and positional parameters of all the three polytypes of In_2O_3 have been found, which are in good agreement with experimental data except for the $I2_13$ phase where the positional parameters deviate from experiment. In_2O_3 in space group of $I2_13$ is found to be a distorted one of space group $Ia\bar{3}$. Upon optimization of the lattice, the former is transformed into the latter structure. The present calculations predicted pressure-induced phase transition from In_2O_3-II to -III. The calculated transition pressure is compared with available experimental values. Based on the analysis of band structure calculated within LDA and GGA, it is found that In_2O_3-III has indirect band gap, whereas In_2O_3-II has direct band gap. Intermediate band is found in In_2O_3-I located right above the valence band, and it is isolated from the valence and conduction bands. From the orbital decomposition analysis and orbital as well as site-projected density of states, the characters of the valence and conduction bands have been analyzed. It is shown that the topmost valence band consists of O $2p$ states hybridized with In $4d$ states. Further, we found that the conduction band minimum of In_2O_3-II consists of In $5s$ orbitals hybridized with O $2s$ orbitals, whereas that for In_2O_3-III is mainly In $5s$ states. From orbital and site decomposed band analysis, it is shown that the topmost valence bands of In_2O_3-II and -III are contributed by electrons from O $2p_x$, $2p_y$, $2p_z$ orbitals slightly hybridized with those from In $4d_{xy}$, $4d_{xz}$, and $4d_{yz}$. Conduction band effective masses are found to be almost isotropic in all the In_2O_3 polytypes. From charge-density, electron localization function, Bader, and Voronoi-charge analyses, it is found that the chemical bonding in In_2O_3 phases has dominant ionic character with noticeable covalency. The magnitudes of the absorption coefficient and reflectivity of In_2O_3 with space groups $Ia\bar{3}$ and $R\bar{3}$ are small in the energy range 0–5 eV; hence, the latter polymorph of In_2O_3 can also be regarded and classified as transparent.

ACKNOWLEDGMENTS

This work has been supported by FUNMAT under Project No. 101043. Supercomputing support was provided through the Research Council of Norway. The authors gratefully acknowledge Ch. Y. Wang (Institute of Micro- and Nanotechnologies, Technical University Ilmenau, Ilmenau, Germany) for fruitful discussions and sending his experimental optical data used for comparison with the present theoretical results. We are thankful to R. Vidya and A. Klaveness for practical help and useful discussions.

[1] H. Kawazoe, M. Yasukawa, H. Hyodo, M. Kurita, H. Yanagi, and H. Hosono, Nature (London) **389**, 939 (1997).
[2] G. Thomas, Nature (London) **389**, 907 (1997).
[3] J. F. Wager, Science **300**, 1245 (2003).
[4] A. N. Banerjee and K. K. Chattopadhyay, Prog. Cryst. Growth Charact. Mater. **50**, 528 (2006).
[5] R. Martins, E. Fortunato, P. Nunes, I. Ferreira, A. Marques, M. Bender, N. Katsarakis, V. Cimalla, and G. Kiriakidis, J. Appl. Phys. **96**, 1398 (2004).
[6] H. Sato, T. Minami, S. Takata, and T. Yamada, Thin Solid Films **236**, 27 (1993).
[7] A. V. Mudryi, A. V. Ivaniukovich, and A. G. Ulyashin, Thin Solid Films **515**, 6489 (2007).
[8] W. Zachariasen, Norsk Geologisk Tidsskrift **9**, 310 (1927).
[9] I. Tanaka, M. Mizuno, and H. Adachi, Phys. Rev. B **56**, 3536 (1997).
[10] M. Sorescu, L. Diamandescu, D. Tarabasanu-Mihaila, and V. S. Teodorescu, J. Mater. Sci. **39**, 675 (2004).
[11] C. Y. Wang, V. Cimalla, H. Romanus, T. Kups, G. Ecke, T. Stauden, M. Ali, V. Lebedev, J. Pezoldt, and O. Ambacher, Appl. Phys. Lett. **89**, 011904 (2006).
[12] B. Yaglioglu, H.-Y. Yeom, and D. Paine, Appl. Phys. Lett. **86**, 261908 (2005).
[13] Y. Mi, H. Odaka, and S. Iwata, Jpn. J. Appl. Phys., Part 1 **38**, 3453 (1999).
[14] H. Odaka, S. Iwata, N. Taga, S. Ohnishi, Y. Kaneta, and Y. Shigesato, Jpn. J. Appl. Phys., Part 1 **36**, 5551 (1997).
[15] O. N. Mryasov and A. J. Freeman, Phys. Rev. B **64**, 233111 (2001).
[16] A. J. Freeman, K. R. Poeppelmeier, T. O. Mason, R. Chang, and T. J. Marks, MRS Bull. **25**, 45 (2000).
[17] P. Erhart, A. Klein, R. G. Egdell, and K. Albe, Phys. Rev. B **75**, 153205 (2007).
[18] T. Tomita, K. Yamashita, Y. Hayafuji, and H. Adachi, Appl. Phys. Lett. **87**, 051911 (2005).
[19] J. C. C. Fan and J. B. Goodenough, J. Appl. Phys. **48**, 3524 (1977).
[20] S. A. Knickerbocker and A. K. Kulkarni, J. Vac. Sci. Technol. A **13**, 1048 (1995).
[21] A. K. Kulkarni and S. A. Knickerbocker, J. Vac. Sci. Technol. A **14**, 1709 (1996).
[22] A. K. Kulkarni and S. A. Knickerbocker, J. Vac. Sci. Technol. A **14**, 757 (1996).
[23] C.-Y. Ren, S.-H. Chiou, and J. Choisnet, J. Appl. Phys. **99**, 023706 (2006).
[24] *Inorganic Crystal Structure Database* (Gmelin Institut, Karlsruhe, 2001).
[25] M. Marezio, Acta Crystallogr. **20**, 723 (1966).
[26] C. T. Prewitt, R. D. Shaxnon, D. B. Rogers, and A. W. Sleight, Inorg. Chem. **8**, 1985 (1969).
[27] G. Kresse and J. Furthmüller, Phys. Rev. B **54**, 11 169 (1996).
[28] J. P. Perdew and A. Zunger, Phys. Rev. B **23**, 5048 (1981).
[29] D. M. Ceperley and B. J. Alder, Phys. Rev. Lett. **45**, 566 (1980).
[30] J. P. Perdew, K. Burke, and M. Ernzerhof, Phys. Rev. Lett. **77**, 3865 (1996).
[31] P. E. Blöchl, Phys. Rev. B **50**, 17 953 (1994).
[32] G. Kresse and D. Joubert, Phys. Rev. B **59**, 1758 (1999).
[33] B. Adolph, J. Furthmüller, and F. Bechstedt, Phys. Rev. B **63**, 125108 (2001).
[34] P. Vinet, J. H. Rose, J. Ferrante, and J. R. Smith, J. Phys.: Condens. Matter **1**, 1941 (1989).
[35] P. Ravindran, A. Delin, B. Johansson, O. Eriksson, and J. M.

Wills, Phys. Rev. B **59**, 1776 (1999).
[36] S. Zh. Karazhanov, P. Ravindran, A. Kjekshus, H. Fjellvåg, and B. G. Svensson, Phys. Rev. B **75**, 155104 (2007).
[37] M. Cardona and G. Harbeke, Phys. Rev. **137**, A1467 (1965).
[38] R. D. Shannon, Solid State Commun. **4**, 629 (1966).
[39] H. R. Hoekstra, Inorg. Chem. **5**, 754 (1966).
[40] T. Wittkowski, J. Jorzick, H. Seitz, B. Schröder, K. Jung, and B. Hillebrands, Thin Solid Films **398-399**, 465 (2001).
[41] I. Hamberg, C. G. Granqvist, K. F. Berggren, B. E. Sernelius, and L. Engström, Phys. Rev. B **30**, 3240 (1984).
[42] J. E. Medvedeva, Phys. Rev. Lett. **97**, 086401 (2006).
[43] R. L. Weiher and R. P. Ley, J. Appl. Phys. **37**, 299 (1966).
[44] M. Anwar, I. M. Ghauri, and S. A. Siddiqi, J. Mater. Sci. **41**, 2859 (2006).
[45] C. McGuinness, C. B. Stagarescu, P. J. Ryan, J. E. Downes, D. Fu, K. E. Smith, and R. G. Egdell, Phys. Rev. B **68**, 165104 (2003).
[46] S. Z. Karazhanov, P. Ravindran, U. Grossner, A. Kjekshus, H. Fjellvåg, and B. G. Svensson, Solid State Commun. **139**, 391 (2006).
[47] M. Orita, H. Sakai, M. Takeuchi, Y. Yamaguchi, T. Fujimoto, N. Fukumoto, and I. Kojima, Hyomen Kagaku **17**, 440 (1996).
[48] T. Barr and Y. L. Liu, J. Phys. Chem. Solids **50**, 657 (1989).
[49] S. Z. Karazhanov, P. Ravindran, U. Grossner, A. Kjekshus, H. Fjellvåg, and B. G. Svensson, J. Appl. Phys. **100**, 043709 (2006).
[50] S. Lalitha, S. Z. Karazhanov, P. Ravindran, S. Senthilarasu, R. Sathyamoorthy, and J. Janabergenov, Physica B **387**, 227 (2007).
[51] W. R. L. Lambrecht, A. V. Rodina, S. Limpijumnong, B. Segall, and B. K. Meyer, Phys. Rev. B **65**, 075207 (2002).
[52] W. R. L. Lambrecht and B. Segall, Phys. Rev. B **52**, R2249 (1995).
[53] K. Kim, W. R. L. Lambrecht, B. Segall, and M. van Schilfgaarde, Phys. Rev. B **56**, 7363 (1997).
[54] S. Z. Karazhanov and L. C. Lew Yan Voon, Semiconductors **39**, 177 (2005).
[55] M. Willatzen, M. Cardona, and N. E. Christensen, Phys. Rev. B **51**, 17992 (1995).
[56] K. Hümmer, Phys. Status Solidi B **56**, 249 (1973).
[57] Y.-N. Xu and W. Y. Ching, Phys. Rev. B **48**, 4335 (1993).
[58] S. H. Brewer and S. Franzen, Chem. Phys. **300**, 285 (2004).
[59] Y. Ohhata, F. Shinoki, and S. Yoshida, Thin Solid Films **59**, 255 (1979).
[60] P. Vajeeston, P. Ravindran, R. Vidya, A. Kjekshus, and H. Fjellvåg, Europhys. Lett. **72**, 569 (2005).
[61] A. D. Becke and K. E. Edgecombe, J. Chem. Phys. **92**, 5397 (1990).
[62] B. Silvi and A. Savin, Nature (London) **371**, 683 (2004).
[63] R. F. W. Bader, *Atoms in Molecules: A Quantum Theory* (Oxford University Press, New York, 1990).
[64] G. Henkelman, A. Arnaldsson, and H. Jónsson, Comput. Mater. Sci. **36**, 354 (2006).
[65] C. F. Guerra, J.-W. Handgraaf, E. J. Baerends, and F. M. Bickelhaupt, J. Comput. Chem. **25**, 189 (2003).
[66] R. D. King-Smith and D. Vanderbilt, Phys. Rev. B **47**, 1651 (1993).
[67] R. Resta, Rev. Mod. Phys. **66**, 899 (1994).
[68] W. R. L. Lambrecht, B. Segall, J. Rife, W. R. Hunter, and D. K. Wickenden, Phys. Rev. B **51**, 13516 (1995).